# Analysis of various haemodynamic parameters in subject-specific carotid bifurcations.

## Rhodri L T Bevan[1], Perumal Nithiarasu[1], Raoul van Loon[1], Igor Sazonov[1] and Heyman Luckraz[2]

**1** College of Engineering, Swansea University
Swansea, UK, R.Bevan@Swansea.ac.uk

**2** Heart and Lung Centre, Royal Wolverhampton Hospital
Wolverhampton, UK

## Abstract

In the present work, the wall shear stress derived haemodynamic wall parameters are investigated on four subject-specific carotid geometries. Two of the four contain a moderate stenosis. Shear stresses have been linked both to atherogenesis (low WSS) and enhanced platelet activation and thrombus formation (very high WSS). This necessitates accurate assessment of the WSS across the spectrum. For this, the current work introduces high near-wall refinement. A semi-autonomous method was utilised to reconstruct the patient geometries. The artificial compressibility form of the characteristic based split scheme is used to solve the unsteady incompressible Navier-Stokes equations. Analysis of the flow is undertaken through the use of six haemodynamic wall parameters which have been brought together from existing literature. The peak time-averaged WSS in two carotids was found to be damaging (467 and 805 dyne/cm$^2$ respectively). Within the two remaining carotids, a potential region of atherogenesis was identified. This region corresponded to the stenotic location of the stenosed carotids.

**Keywords:** human carotid bifurcation, wall shear stress, haemodynamic wall parameters, computational fluid dynamics.

## Introduction

Diseases of the heart and circulatory system (cardiovascular disease or CVD) are the main cause of death in Europe, the United States and regions of Asia. In the UK, they accounted for almost 191,000 deaths in 2008, which is one in three of all deaths [1]. Clinical observations have demonstrated that atherosclerosis typically occurs at regions of complex haemodynamics such as arterial bifurcations or regions of high curvature. In the present work, subject-specific modelling of the carotid bifurcation is undertaken from patients that have been clinically diagnosed with a diseased carotid artery. Four carotids from three patients are examined in the work.

Research has determined that low or oscillatory wall shear stress (WSS) is associated with atherogenesis [10, 24, 32, 39]. The work of Cheng *et al* [8] investigated the influence of both low and oscillatory shear stress on atherosclerotic plaque formation within mouse carotid arteries. They concluded that while both low and oscillating shear stresses induce atherosclerotic lesions to develop, the composition of the plaque was dependent on whether low shear stress was encountered individually or in combination with oscillatory shear.

In contrast, high shear stress has been shown to induce mechanical and/or chemical mechanisms that work in concert to provide athero-protective effects [3, 4, 17, 18, 31].

Traub *et al* [46] determined that steady laminar shear promotes the release of secreted factors that inhibit coagulation and smooth muscle cell production while also suppressing leukocyte adhesion and transmission. Turbulent or oscillatory shear stresses increase endothelial cell turnover while sustained laminar shear stresses are required for optimum repair of the endothelial cells.

However, when plaque formation is in progress, the artery narrows forming a stenosis. Under stenotic flow conditions, low wall shear stress is no longer prevalent although growth is ongoing. Clinical studies such as [16, 40] have shown that high WSS is also linked to platelet activation and thrombus formation. Mailhac *et al* [28] also concluded that fibrin(ogen) and platelet deposition is maximal at the apex of a stenosis and coincident to high shear stress on a damaged arterial wall. In the work of Groen *et al* [11], a case study of a carotid artery is outlined where plaque rupture occurs at the location of high shear stress. This highlights the need to accurately assess the WSS throughout the plaque development cycle.

A limited number of numerical studies are available on flow through carotid bifurcations, typically utilising WSS derived haemodynamic wall parameters (HWPs) for analysing the flow over the cardiac cycle [10, 19, 26, 49]. It is known that capturing and converging WSS requires good boundary layer meshes. However, only one of the stud-

ies reported in this area mentions boundary refinement. In this paper, we introduce structured boundary layer refinement to capture the high near-wall velocity gradients. The investigations in [47] quantified the relationship between several derived HWPs and the carotid intima-media thickness (IMT). Research has also shown that the carotid IMT is an indicator of atherogenesis [6, 9].

In this work, six haemodynamic wall parameters are brought together and investigated. These are the time-averaged wall shear stress (WSSTA), time-averaged wall shear stress spatial gradient (WSSG), maximum wall shear stress temporal gradient (WSSTG), the oscillatory shear index (OSI), wall shear stress angle deviation (WSSAD) and wall shear stress angle gradient (WSSAG).

The six parameters were brought together for the first time in [5] for the high resolution simulation of blood flow through a healthy carotid bifurcation. In the present work, we expand the six parameter combined investigation to consider high resolution simulations of both healthy and diseased carotid bifurcations.

The remaining paper is arranged into the following sections. The section that follows the introduction provides a brief outline of the mesh reconstruction methodology. In next sections, we highlight the fluid dynamics algorithm used together with the construction of the flow profile. The final sections provide a detailed discussion on the results obtained before some conclusions on the study are drawn.

## Mesh Construction

The geometries were reconstructed from sets of CT images. The carotid geometries (left and right from each patient) were reconstructed from sets provided by Royal Wolverhampton Hospital, Wolverhampton, UK. Scan resolution was $0.35 \times 0.35$mm in the slice plane and 0.5mm between the slices. The sets consisted of approximately 500-600 slices. At least one of the carotids in each of the Wolverhampton sets has been clinically diagnosed with a stenosis.

Two techniques were utilised for the reconstruction process. In the first, geometric reconstruction was undertaken using AMIRA. The second approach was developed to remove inter-user variability within geometry reconstruction. In this alternative approach, the subject-specific geometries were reconstructed using an in-house semi-autonomous method [43]. The first step in the process was image segmentation. This was undertaken using a level set method consisting of an implicit deformable model along with an external force field called the geometric potential force (GPF). Once completed, the binary voxel image is converted into an initial surface mesh using the Marching Cube method. In order to improve the surface mesh provided by either approach, surface coarsening and smoothing using the technique given by Saksono *et al* [41] was undertaken.

As mentioned, the wall shear stress derived parameters investigated need a high resolution meshing scheme along the vessel wall in order to capture the high velocity gradient close to the wall [5]. To construct these layers, the

surface mesh nodes are projected inward and points are placed at a specific distance in the direction of the inward surface normal. A new inside surface mesh is constructed from these new points, creating a surface mesh with the same topology as the outer wall surface mesh. Prisms are then formed between corresponding surface faces. Multiple prismatic layers can be formed in this way. To generate the volume mesh inside the structured layers, every prism is first divided into a number of shorter prisms. To do this, every edge connecting the two triangles is divided into shorter sides using geometrical progression with smaller size edges placed close to the wall. Then, every prism is the divided into three tetrahedra. The geometrical progression employed is determined by the following technique.

Let $d$ be the mean size of the surface element face and the inner prismatic layer thickness be $d \times f$ where $f$ is a diminishing factor. The thickness of a prismatic layer from inside the geometry to the solid surface is reduced by a factor $f$ progressively. Thus the total depth $D$ of the boundary layer (comprised of $N$ layers) is defined as:

$$D = df + df^2 + df^3 + ... + df^N \qquad (1)$$

with $df^N$ being the thickness of the layer adjacent to the wall. In order to produce a solution, either $D$ or $f$ must be specified. For meshes involving less than 6 boundary layers, the total depth was defined as $D = 2d$. For meshes with more than six boundary layers, the factor $f$ is defined using the equation

$$f = \frac{N^a}{N^a + 1} \qquad (2)$$

where $a = 0.452$ was chosen to provide continuity for a six layered mesh between the two techniques. The distribution employed allows for a smooth transformation between the inner unstructured mesh and the boundary layer mesh.

Table 1 depicts the prismatic layer distribution for increasing $N$. The thinnest prismatic layer has a thickness of $df^N$. Thus the $f^N$ column in the table quantitively highlights the increasing density of the mesh at the solid surface. Figure 1 illustrates the boundary layer mesh distribution used in the present study against cumulative distance (depth) from the inner mesh. The depth is defined relative to the average surface element size $d$.

With the construction of boundary layers, the inlet and outlet surfaces of the geometry also now contains these structured layers. Beyond the inner structured layer surface, the surface mesh at inlet/exit is generated using the unstructured methodology referred to as stitching method [42]. This provides a high quality surface mesh at inlet/exit, as shown in Figure 2.

The boundary layer technique also takes into account the relative shape of the surface mesh, through modification of the boundary layer depths. This ensures that there is no crossing/overlap between the inner and outer surface meshes when projecting along the surface inner normals

| No of layers (N) | $f$ | $D/d$ | $f^N$ |
|---|---|---|---|
| 3 | 0.8105 | 2.00 | 0.5324 |
| 4 | 0.7413 | 2.00 | 0.3020 |
| 5 | 0.7090 | 2.00 | 0.1792 |
| 6 | 0.6921 | 2.00 | 0.1099 |
| 7 | 0.7067 | 2.20 | 0.0881 |
| 8 | 0.7191 | 2.38 | 0.0715 |
| 9 | 0.7297 | 2.54 | 0.0587 |
| 10 | 0.7390 | 2.69 | 0.0486 |
| 11 | 0.7472 | 2.84 | 0.0405 |
| 12 | 0.7546 | 2.97 | 0.0341 |

**Table 1 Table of prismatic layer properties.**

**Figure 1 Flow through a patient-specific carotid bifurcation. For a mesh with N prismatic layers, the cumulative inter-layer depths (relative to $d$).**
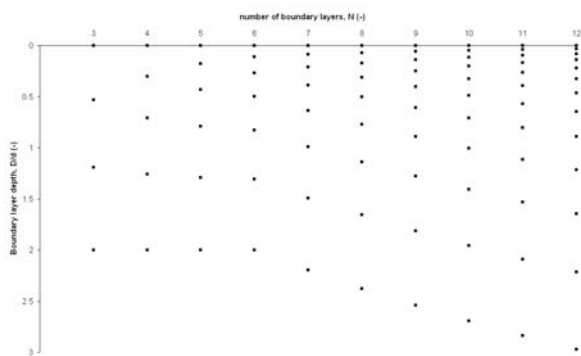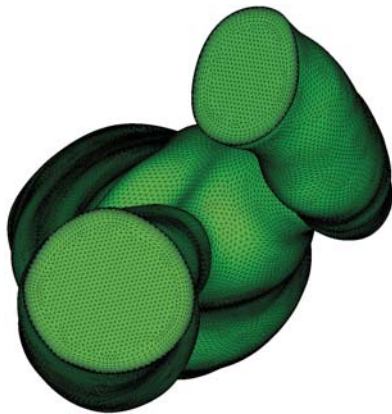


**Figure 2 Closeup of Patient 01 right carotid artery mesh outlet with boundary layers.**



(for example proximal to a stenosis). This process is outlined in detail in [43]. The volume tetrahedron mesh of the remaining domain is generated using the Delaunay triangulation method described in [13, 48].

The mesh geometries are provided in Figure 3. All of the mesh geometries contained 10 structured boundary layers. The choice of ten boundary layers was based upon a prior mesh convergence study [5]. The mesh for Patient 1 right carotid consisted of 6,934,199 linear tetrahedral elements and 1,185,109 nodes. The right carotid mesh for Patient 2 consisted of 6,111,472 elements and 1,047,301 nodes. The left carotid mesh for Patient 02 consisted of 4,126,777 linear tetrahedral elements and 708,191 nodes. The left carotid in Patient 3 had a more complicated and longer structure and the reconstructed mesh consisted of 13,124,417 elements and 2,239,739 nodes.

**Figure 3 Carotid Mesh Geometries for Patient 1 right (P01R), Patient 2 right (P02R), Patient 2 left (P02L) and Patient 3 left (P03L).**
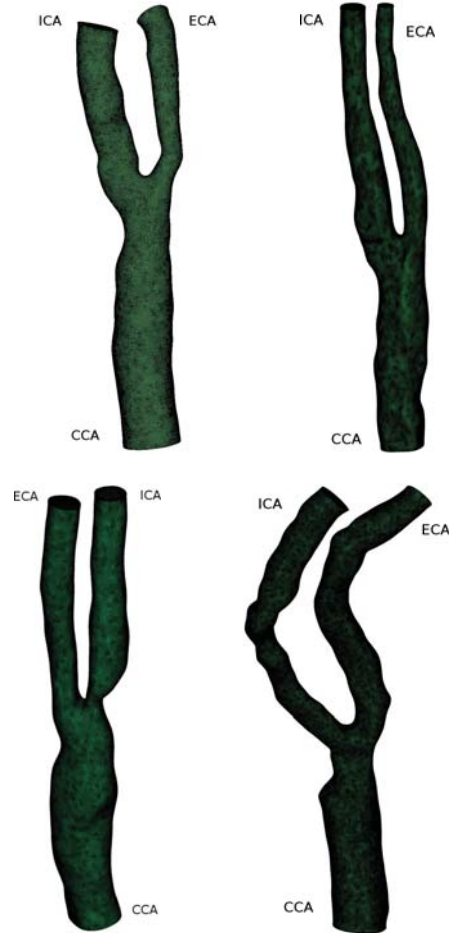


From Figure 3, it can be seen that the geometries for the right carotids of Patient 1 and 2 display some of the standard features expected within a carotid bifurcation. Namely, the internal carotid artery (ICA) diameter is greater than that of the external carotid artery (ECA) and in the Patient 2 right carotid the ICA narrows after the bifurcation (carotid sinus or bulb feature). The Patient 2 right carotid displays a smooth transition along its entire length (within the domain), whereas the Patient 1 right carotid has a sharp feature downstream of the bifurcation in the ECA. The left carotid of Patient 2 has a stenosis which occludes approximately 65% of the ICA. The left carotid in Patient 3 displayed less regular features due to calcification which can be clearly seen immediately upstream of the bifurcation.

## Governing Equations

The artificial compressibility based Navier-Stokes equations may be written as

*Continuity*

$$\frac{1}{\beta^2}\frac{\partial p}{\partial t} + \rho\frac{\partial u_i}{\partial x_i} = 0 \tag{3}$$

*Momentum*

$$\frac{\partial u_i}{\partial t} + u_j\frac{\partial u_i}{\partial x_j} + \frac{1}{\rho}\frac{\partial p}{\partial x_i} - \frac{1}{\rho}\frac{\partial \tau_{ij}}{\partial x_j} = 0 \tag{4}$$

where $u_i$ are the cartesian components of the velocity vector, $\rho$ is the fluid density, $p$ represents the pressure and $\beta$ is an artificial compressibility parameter [33, 37, 52]. The deviatoric stress components $\tau_{ij}$ are related to the velocity gradients by

$$\tau_{ij} = \mu\left(\frac{\partial u_i}{\partial x_j} + \frac{\partial u_j}{\partial x_i} - \frac{2}{3}\frac{\partial u_k}{\partial x_k}\delta_{ij}\right) \tag{5}$$

Non-dimensional forms of the equations are used, along with appropriate reference quantities [33]. The problem definition is completed by selecting appropriate initial and boundary conditions.

## The characteristic based split (CBS) scheme

The characteristic based split (CBS) scheme is a well established algorithm for both incompressible and compressible flow simulations [35, 50–52]. The artificial compressibility form has been incorporated into the CBS family since 2003 [33, 34, 37]. The CBS scheme consists of three steps. In the first step, a solution to an intermediate velocity field is determined. The second step uses the continuity (pressure) equation to calculate the pressure field. In the third step, the intermediate velocity field is then corrected to give the final velocity values.

The three steps are defined (semi-discrete, non-dimensional form) as:

1. Calculate the intermediate velocity field, $u_i^\dagger$

$$\begin{aligned}\frac{u_i^\dagger - u_i^n}{\Delta t} &= -\left(\frac{\partial u_j u_i}{\partial x_j}\right)^n + \frac{\partial}{\partial x_j}\left(\frac{1}{Re}\frac{\partial u_i}{\partial x_j}\right)^n \\ &+ \frac{\Delta t}{2}u_k\frac{\partial}{\partial x_k}\left(\frac{\partial u_j u_i}{\partial x_j}\right)^n\end{aligned} \tag{6}$$

the higher order terms are due to characteristic time discretisation [52].

2. Solve for the pressure field, $p^{n+1}$

$$\frac{1}{\beta^2}\frac{p^{n+1} - p^n}{\Delta t} = -\rho\frac{\partial}{\partial x_i}\left(u_i^\dagger - \Delta t\left(\frac{\partial p}{\partial x_i}\right)^n\right) \tag{7}$$

3. Solve for the corrected velocity field, $u_i^{n+1}$

$$u_i^{n+1} = u_i^\dagger - \Delta t\left(\frac{\partial p}{\partial x_i}\right)^n + \frac{\Delta t^2}{2}u_k\frac{\partial}{\partial x_k}\left(\frac{\partial p}{\partial x_i}\right)^n \tag{8}$$

Equations 6-8 can now be spatially discretised. For further details, refer to [5]. The artificial compressibility parameter $\beta$ is determined locally, based on both convective and diffusive time-step restrictions [33, 36, 52]. Local determination makes the scheme suitable for different flow regimes (convection and diffusion dominated) within a problem at a particular Reynolds number. In this work the relation

$$\beta = \max\left(\epsilon, \nu_{conv}, \nu_{diff}\right) \tag{9}$$

is employed. The constant $\epsilon$ ensures that $\beta$ does not approach zero, and typically takes the value of $0.1 \leq \epsilon \leq 0.5$. $\nu_{conv}$ is the local convective velocity and $\nu_{diff}$ is the local diffusive velocity. These velocities are calculated from the non-dimensional relations [33],

$$\nu_{conv} = \sqrt{u_i u_i} \tag{10}$$

$$\nu_{diff} = \frac{1}{hRe} \tag{11}$$

Local time-stepping [52] is employed as an iteration mechanism to accelerate convergence to a solution and provide optimal stabilisation. The local time step is calculated as

$$\Delta t = \frac{h}{\|\mathbf{u}\| + \beta} \tag{12}$$

The calculated local time step is multiplied by a safety factor varying between 0.1 and 1.0 depending on the problem and mesh employed.

With the use of local time-stepping, a dual time-stepping mechanism is required to recover the transient solution. A real time-step term is introduced into the momentum equation, which is applied to Step 3 [33, 35]. The addition of this term leads to the modified third step equation in the form of

$$\begin{aligned}u_i^{n+1} &= u_i^\dagger - \Delta t\left(\frac{\partial p}{\partial x_i}\right)^n \\ &+ \frac{\Delta t^2}{2}u_k\frac{\partial}{\partial x_k}\left(\frac{\partial p}{\partial x_i}\right)^n + \Delta t\frac{\Delta u_{i\tau}}{\Delta \tau}\end{aligned} \tag{13}$$

where $\Delta \tau$ is the real time step. In order to achieve third-order real time accuracy, $\Delta u_{i\tau}$, is approximated as

$$\Delta u_i^\tau = \frac{11u_i^n - 18u_i^{m-1} + 9u_i^{m-2} - 2u_i^{m-3}}{6} \tag{14}$$

In the above equations the nth term denotes the solution from the previous pseudo time step and mth term denotes the solution from the respective mth real time level. The mth terms need to be appropriately stored at the start of each real time level. Due to the implicit nature of the baward difference formula, no time step restrictions are placed on the real time step.

The instantaneous steady state has been achieved, for the current real time-step, when the $L_2$ residual norm of the velocity has reduced to $10^{-5}$.

## Boundary conditions

The blood dynamic viscosity and density are taken to be $\mu = 0.0035$ kg/m s and $\rho = 1.0 \times 10^3$ kg/m$^3$ respectively. A no-slip boundary condition was applied to the vessel wall. Without subject-specific velocity profiles, an alternative approach is considered. There are several possible flow profiles that can be employed within the field of blood flow modelling for the inflow and outflow boundaries. A Womersley profile, which assumes fully developed unsteady flow is widely used in the field [2, 10, 22, 25, 45, 49]. The Womersley profile is a 2D linear viscous solution of the Navier-Stokes equations for cylindrical tubes. A mapping procedure must be undertaken to map the flow profile to a non-circular cross section, introducing a small error dependent on the non-circularity of the inlet/outlet. In this work, an alternative method is employed to determine the velocity profile. This numerical solution assumes a constant cross-sectional area along a straight pipe to determine the solution. The cross-section is not required to be circular. In straight pipe flow, the Navier-Stokes equations reduce to a single linear parabolic inhomogeneous PDE with respect to the axial velocity component $u(x, y, t)$

$$\frac{\partial u}{\partial t} + \nu \frac{\partial^2 u}{\partial x_1^2} + \nu \frac{\partial^2 u}{\partial x_2^2} = \frac{1}{\rho} \frac{\partial p(t)}{\partial x_3} \qquad (15)$$

Since the PDE is linear, the pressure and solution can be represented by a Fourier series (assuming $\frac{\partial p(t)}{\partial x_3}$ is periodic).
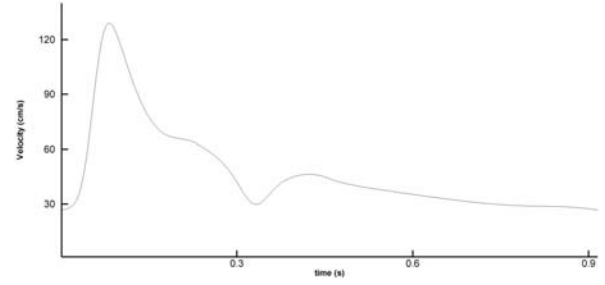
$$\frac{\partial p(t)}{\partial x_3} = \sum_{n=-\infty}^{+\infty} \left( \frac{\partial \tilde{p}}{\partial x_3} \right)_n e^{i\omega_n t} \qquad (16)$$

where $\omega_n = 2\pi n/T$. Examining the harmonics individually and representing the velocity $u(x, y, t) = \tilde{u}(x, y)e^{i\omega_n t}$ gives

$$i\omega \tilde{u} + \nu \frac{\partial \tilde{u}}{\partial x_1} + \nu \frac{\partial \tilde{u}}{\partial x_2} = \frac{1}{\rho} \frac{\partial \tilde{p}}{\partial x_3} \qquad (17)$$

This is the Helmholtz equation, and ignoring ˜ may be rewritten as

**Figure 4 The carotid waveform constructed from the harmonics in Table 2.**



$$\frac{\partial^2 u}{\partial x_1} + \frac{\partial^2 u}{\partial x_2} + k^2 u = f \qquad (18)$$

where $k^2 = \frac{i\omega}{\nu}$ and $f = \frac{1}{\eta} \frac{\partial p}{\partial x_3}$. The numerical solution can now be determined using the Finite Element method and noting that on the boundary $u = 0$. The harmonics utilised to construct the waveform are given in Table 2. The waveform is shown in Figure 4.

**Table 2 Harmonics utilised to construct the carotid waveform**

| Harmonic | freq. (Hz) | Amplitude (cm) | phase (rad) |
|---|---|---|---|
| 0 | 0.0000000 | 46.926373 | 0.0000000 |
| 1 | 1.0875476 | 21.524133 | -1.1757456 |
| 2 | 2.1750952 | 17.614591 | -1.6399569 |
| 3 | 3.2626427 | 12.147710 | -2.4126155 |
| 4 | 4.3501903 | 6.7678515 | -2.5923204 |
| 5 | 5.4377379 | 9.0132960 | -2.8654415 |
| 6 | 6.5252855 | 8.0155307 | 2.5792239 |
| 7 | 7.6128331 | 4.4200926 | 2.0271286 |
| 8 | 8.7003806 | 3.5711419 | 1.9278901 |
| 9 | 9.7879282 | 3.4320565 | 1.3878100 |
| 10 | 10.875476 | 2.3272178 | 0.77936298 |
| 11 | 11.963023 | 1.4287817 | 0.62628156 |
| 12 | 13.050571 | 1.5817702 | 0.35279629 |
| 13 | 14.138119 | 1.2964663 | -0.36075375 |
| 14 | 15.225666 | 0.71691449 | -0.75219771 |
| 15 | 16.313214 | 0.64928471 | -0.87984983 |
| 16 | 17.400761 | 0.55890994 | -1.4506194 |
| 17 | 18.488309 | 0.35656742 | -1.8778747 |
| 18 | 19.575856 | 0.27656662 | -2.0518077 |
| 19 | 20.663404 | 0.25371520 | -2.4611692 |
| 20 | 21.750952 | 0.18540847 | -2.9991421 |
| 21 | 22.838499 | 0.11846889 | 3.0061654 |
| 22 | 23.926047 | 0.10273053 | 2.7403593 |
| 23 | 25.013594 | 0.077012238 | 2.2301464 |
| 24 | 26.101142 | 0.049128254 | 1.9239422 |

In the situation where the arterial cross-section varies significantly the vessel wall faces may not be orthogonal to the inlet or outlet. In this case, it may be necessary to use a combing technique to adjust the velocity vectors in order to avoid parasitic flow separation. The combing technique, which can be seen as an alternative to the introduction of mesh extensions such as cylinders, can be outlined (see Figure 5) as follows:

- Compute the normal vectors to the wall on outlet/wall shared nodes (green arrows).

**Figure 5 Combing Procedure shown in 2d with exaggerated non-orthogonal wall/inlet angle. Arrows represent vector directions. a) pre-combing b) post-combing**
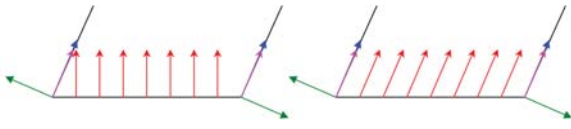


- From the normal vectors, determine the tangental vectors to the wall in the shared nodes (blue arrows).

- Set the initial vectors for the remaining outlet nodes as the outlet normal (red arrows)

- Perform iterations similar to Laplace smoothing, with the shared node normals (pink arrows) being fixed at their initial values, until normals are combed

- Once combed, the velocity vectors are scaled in order to maintain the original flow rate across the arterial cross-section
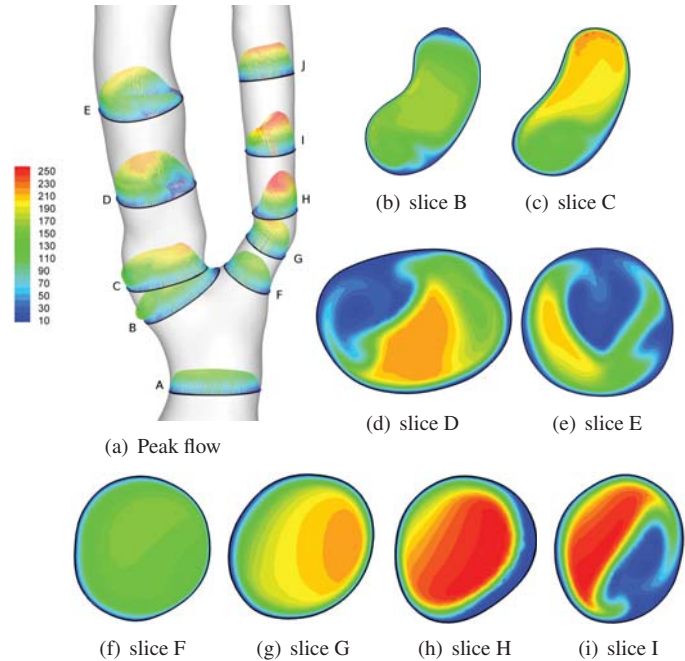
The flow rate ratios at the outlets (ICA and ECA) vary in the literature from constant to non-uniform ratios in time [29, 30, 32]. Milner *et al* [30] concludes that while flow differences do play a role, geometry is the key influence. Therefore in order to simplify the boundary conditions, we have assumed an ICA flow rate of 60% and an ECA flow rate 40% of the total CCA flow rate for healthy geometries. While the left carotid of Patient 2 has a moderate stenosis (65%), this is not typically sufficient to alter the flow distribution between the internal and external carotid arteries [12].

Numerical solutions to the Helmholz equation produced velocity profiles which were applied to both the inlet and the two outlets. The inlet mean flow rate for Patient 1 was set to 4.5cm$^3$/s, which produced a peak velocity at the inlet of 96cm/s. This was chosen based on the accompanying ultrasound data which had a peak velocity of 87cm/s in the CCA although the radius and location were not known. Thus, while the ultrasound data was available, its usefulness was marginal. The mean flow rate at the inlet for Patient 3 was also chosen to be 4.5cm$^3$/s which gave a peak inlet velocity of 71cm/s which again was similar to the ultrasound data of 73cm/s. There was no ultrasound data for Patient 2, so a peak centreline velocity of 101cm/s was assumed for both carotids as this fell in the middle of the range (68-171cm/s) found by Holdsworth *et al* [15]. The cardiac cycle was decomposed into 240 real time steps in each case.

## Results and discussions

During a cardiac cycle, the flow within the carotid bifurcation demonstrates varying complexity which is dependent upon the arterial geometry. Examining the P01R bifurcation during peak flow (Figure 6), it is possible to see the flow has split and many of the velocity profiles are increasingly skewed towards one wall in the ECA and

**Figure 6 Flow at the bifurcation of P01R during peak flow. a) 3D slice representation at peak flow, b) to i) Velocity magnitude and distribution at the respective slice.**



(a) Peak flow

(b) slice B  (c) slice C

(d) slice D  (e) slice E

(f) slice F  (g) slice G  (h) slice H  (i) slice I

ICA due to the curvature effects from the wall with progression downstream. The maximum predicted velocity magnitude in the ECA is 259cm/s for the selected slices and 271cm/s overall. These values are in close agreement with the recorded ultrasound results for the patient. In the ultrasound, the peak velocity in the cardiac cycle varies from 250cm/s to 280cm/s. The peak predicted velocity in the ICA (214cm/s) is higher than the ultrasound value of 181cm/s. However, the difference between the values is reduced closer to the bifurcation. From the obtained values, the choice of 60:40 flow division is acceptable.

Examining the left carotid of patient 3 during peak flow (Figure 7), the skewing effect of the geometrical curvature is pronounced. The maximum velocity in slice A is 144cm/s. This value in the CCA is high considering the peak inlet velocity is only 71cm/s due to the relatively large arterial diameter. The vessel diameter proximal to slice A is constricted by calcification. The ICA for this patient is rather narrow, relative to the ECA. As such, slice D in the ICA experiences the overall peak velocity for the selected slices, and all slices experience velocities greater than 140cm/s. A peak velocity of 164cm/s is predicted. While the ECA is relatively large the flow is concentrated by the curvature effects leaving 30-40% of slice F with velocities of <10cm/s.

The wall shear stress derived haemodynamic wall parameters are utilised to summarise the flow effects on the arterial wall over the entire cardiac cycle. As mentioned previously, low wall shear stress (WSS) is one of the indicators to the location of atheroma. The traction vector $\mathbf{t}$ is calculated from the Cauchy stress tensor $\boldsymbol{\sigma}$ and the surface normal vector $\mathbf{n}$ using

**Figure 7 Flow at the bifurcation of P04L during peak flow. a) 3D slice representation at peak flow, b) to h) Velocity magnitude and distribution at the respective slice.**



(a) Peak flow

(b) slice A    (c) slice B

(d) slice C    (e) slice D

(f) slice E    (g) slice F    (h) slice G
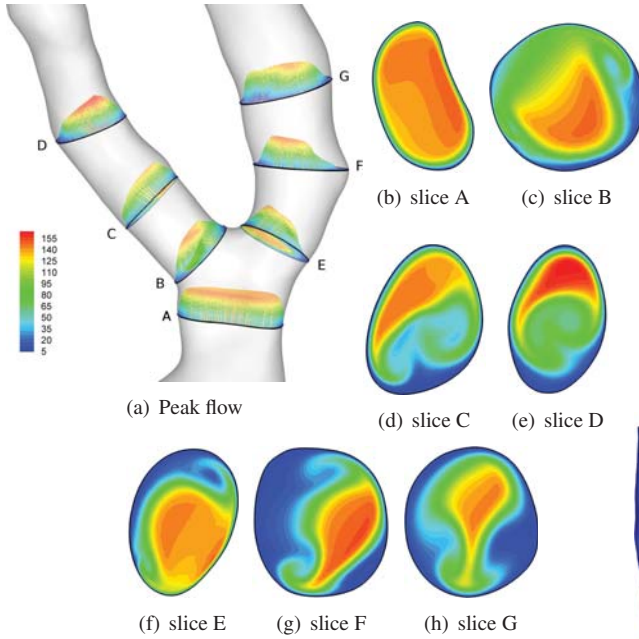
$$\mathbf{t} = \boldsymbol{\sigma} \cdot \mathbf{n} \qquad (19)$$

The surface traction vector $\mathbf{t_s}$ is calculated from

$$\mathbf{t_s} = \mathbf{t} - (\mathbf{t} \cdot \mathbf{n})\mathbf{n} \qquad (20)$$

The time-averaged wall shear stress (WSSTA), $\tau_{abs}$, is expressed as

$$\tau_{abs} = \frac{1}{T} \int_0^T \|\mathbf{t_s}\| \, dt \qquad (21)$$

The WSSTA for the four carotid geometries is presented in Figure 8. From the figure, it is clear that the flow divider experiences high time-averaged WSS in all the carotid simulations. Only P01R and P03L are predicted to experience a peak WSS at the apex. The peak time-averaged WSS in P02R and P03L is located in the ECA and ICA respectively. In P01R, the peak time-averaged WSS is 467 dyne/cm$^2$. The peak value is located proximal to both the flow divider and the stenosis, inducing a higher time-averaged WSS than would otherwise be expected. Proximal to the flow divider, a band of high time-averaged WSS extends across the ECA entrance. Within this band, the time-averaged WSS values range from 100-180 dyne/cm$^2$, with a localised region experiencing a peak of 304 dyne/cm$^2$. These values and their location are in good agreement with the results of Younis et al [49]. Within the CCA, the time-averaged WSS values typically range between 10-25 dyne/cm$^2$ which is greater than the 5-10 dyne/cm$^2$ believed to stimulate an atherosclerosis inducing phenotype. Only in the CCA does a small region experience a WSSTA of less than 5 dyne/cm$^2$.

**Figure 8 WSSTA distribution. (a,b) P01R, (c,d) P02R, (e,f) P02L, (g,h) P03L.**



(a)    (b)    (c)    (d)

(e)    (f)    (g)    (h)
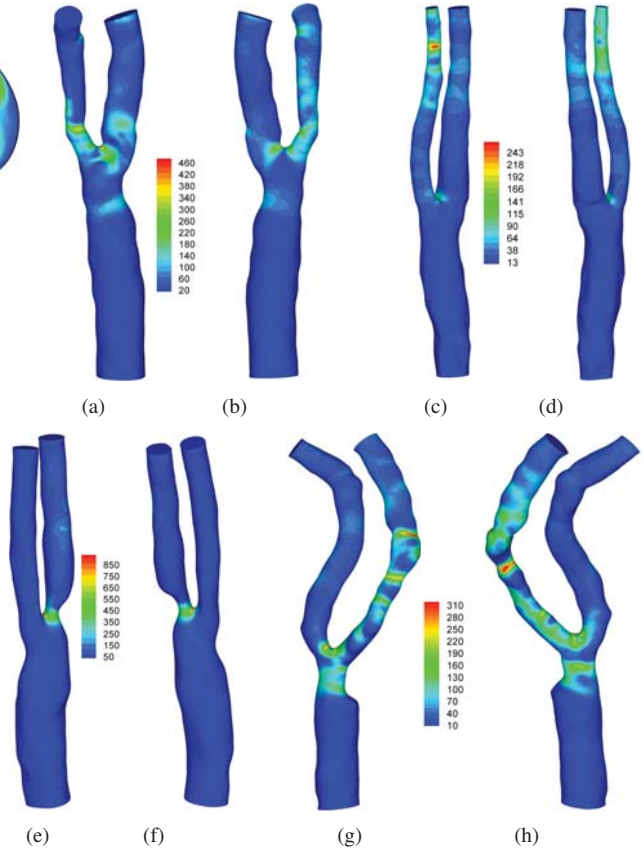
At the bifurcation of P02R, the localised peak time-averaged WSS is predicted to be 143 dyne/cm$^2$. The region of high WSS is located at the flow divider and closer to the inner wall of the ECA. The peak WSSTA predicted for P02R is 269 dyne/cm$^2$, proximal to a small local narrowing in the ECA and influenced by arterial curvature. In contrast to P01R, a significant percentage (approx 40%) of the CCA experiences less than 5 dyne/cm$^2$ and virtually all values in CCA are less than 10 dyne/cm$^2$. A region distal to the flow divider and along the outer wall of the ICA also experiences time-averaged WSS of less than 5 dyne/cm$^2$.

As expected, the peak WSSTA for P02L occurs at the flow divider, although closer to the ICA. The predicted peak of 805 dyne/cm$^2$ is exceptionally high and damaging. Upstream of the stenosis apex lies a band across the ICA of very high time-averaged WSS (400-500 dyne/cm$^2$). This is also greater than the 315 dyne/cm$^2$ that Holme et al [16] determined was sufficient to induce platelet activation and enhanced platelet thrombus formation. Immediately downstream of the stenosis lies a small region experiencing time-averaged WSS of less than 5 dyne/cm$^2$. This is indicative of potentially further plaque formation and corresponds to the region experiencing flow separation. In the CCA, approximately 20% is predicted to experience time-averaged WSS of less than 5 dyne/cm$^2$.

For P03L, the peak WSSTA at the bifurcation is located

nearer to the inner wall of the ECA and a localised region exceeds 250 dyne/cm$^2$. Regions of high WSSTA are concentrated downstream of local narrowing, with the peak of 318 dyne/cm$^2$ occuring in the ICA at a stenosis (30-35% change in diameter). In the CCA, a significant region experiences potentially atherosclerotic inducing low WSSTA. In the ECA however, only a small region experiences this low time-averaged WSS. Like the region predicted for P02R, this is along the outer wall. The majority of the ECA experiences between 10-25 dyne/cm$^2$.

From the four carotids, the CCA typically experiences lower time-averaged WSS values compared to the ECA and ICA. Two of the four carotids have a stenosis along the outer wall of the larger of either the internal or external carotid artery. For the remaining two carotids, the corresponding region experiences low WSS and are potential regions for plaque formation. This is in good qualitative agreement with that of Kaazempur-Mofrad *et al* [20] who found this occurred in three out of four patients. In their work, they theorised that the remaining patient did not experience a corresponding region of low shear stress due to a sudden constriction immediately distal to the bifurcation.

The wall shear stress temporal gradient (WSSTG) is calculated by determining the temporal gradient between instantaneous wall shear stresses for every consecutive time step and storing the maximum value.

$$WSSTG_i = \max\left(\frac{\partial \|\mathbf{t_s}\|_i}{\partial t}\right) = \max\left(\frac{\|\mathbf{t_s}\|_i^{n+1} - \|\mathbf{t_s}\|_i^n}{\Delta t}\right)$$

(22)

where $i$ is the spatial point in question and $0 < t < T$.

The WSSTG is given in Figure 9 for the four carotids. From the figure it is clear that the distribution of WSSTG is in good agreement with that of the time-averaged WSS distribution for P02R and P02L. However, the distributions within P01R and P03L contain significant differences. At the apex of P02R, the peak predicted WSSTG is 15000 dyne/cm$^2$s. In the ECA, however, the WSSTG values exceed 10000 dyne/cm$^2$s in approximately 30% of the artery, with an overall predicted peak of 39000 dyne/cm$^2$s. In [20], values in excess of 40000 dyne/cm$^2$s are encountered in the diseased carotids. In the carotid of P01R, the regions of high time-averaged WSS correspond with regions of high WSSTG. The predicted peak value in the P01R carotid is 70100 dyne/cm$^2$s. At the ICA outlet, the high values are the result of imposing the flow profile and are ignored here. While the differences between WSSTA and WSSTG are localised to the ICA for P01R, significant differences exist between the two distributions in the carotid P03L for all three arteries. In the CCA of P03L, the majority experiences less than 2500 dyne/cm$^2$s which is in good agreement with [49]. In contrast only 10-15% of the ICA experiences a maximum WSSTG of less than 5000 dyne/cm$^2$s. At the bifurcation, the peak WSSTG value exceeds 40000 dyne/cm$^2$s, while the maximum predicted values occur in four small regions of the



Figure 9 WSSTG distribution. (a,b) P01R, (c,d) P02R, (e,f) P02L, (g,h) P03L.
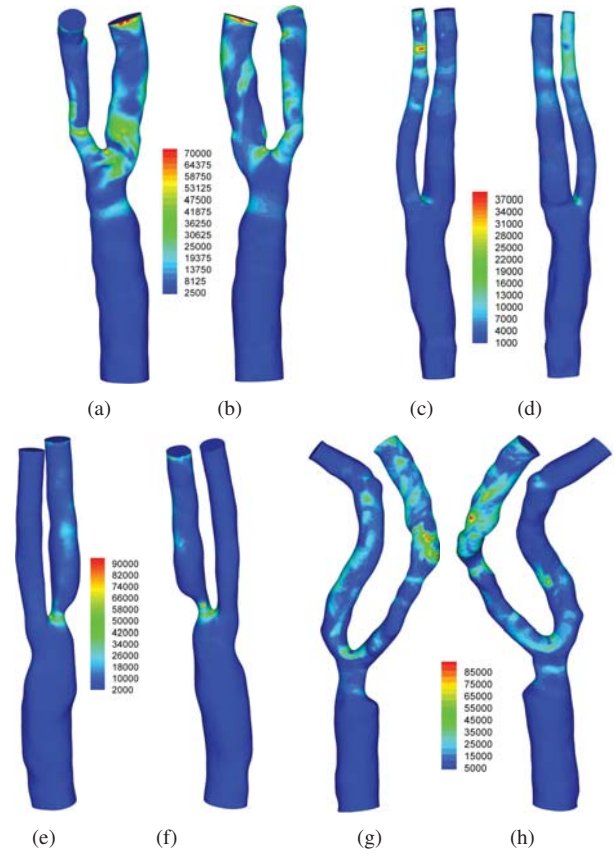
ICA. Each exceeds 85000 dyne/cm$^2$s, with the peak being 95100 dyne/cm$^2$s. This is marginally higher than the peak WSSTG value of 93800 dyne cm$^{-2}$s$^{-1}$ predicted for P02L.

With the work of Vermeersch *et al* [47] finding a negative correlation between high WSSTG and intima media thickness for both the ICA and the CCA, the predicted WSSTG distributions for the four carotids indicate the CCA is at risk of increased intima media thickening since all experience low (defined as less than 2500 dyne cm$^{-2}$s$^{-1}$) WSSTG values. Outside of the CCA, the low WSSTA regions of P02R and P03L also experience low WSSTG.

The time-averaged wall shear stress spatial gradient (WSSG) is intended to identify the areas of locally disturbed flow. $\nabla\mathbf{t_s}$ is an asymmetric tensor with components acting in different directions at a given time point. The magnitudes of the diagonal components of $\nabla\mathbf{t_s}$ dominate [23, 27], thus the time-averaged WSSG is defined as [7]

$$WSSG = \frac{1}{T}\int_0^T \sqrt{\left(\frac{\partial\tau_x}{\partial x}\right)^2 + \left(\frac{\partial\tau_y}{\partial y}\right)^2 + \left(\frac{\partial\tau_z}{\partial z}\right)^2}\,dt$$

(23)

where $\tau_x$ is the $x$-coordinate component of the instantaneous shear stress vector $\mathbf{t_s}$. Since both positive and neg-

ative gradients contribute to atherogenesis, the absolute value of the instantaneous WSSG is employed [23, 27]. High WSSG values indicate sustained acceleration and deceleration of the flow.

**Figure 10 WSSG distribution. (a,b) P01R, (c,d) P02R, (e,f) P02L, (g,h) P03L.**



(a)          (b)          (c)          (d)

(e)          (f)          (g)          (h)
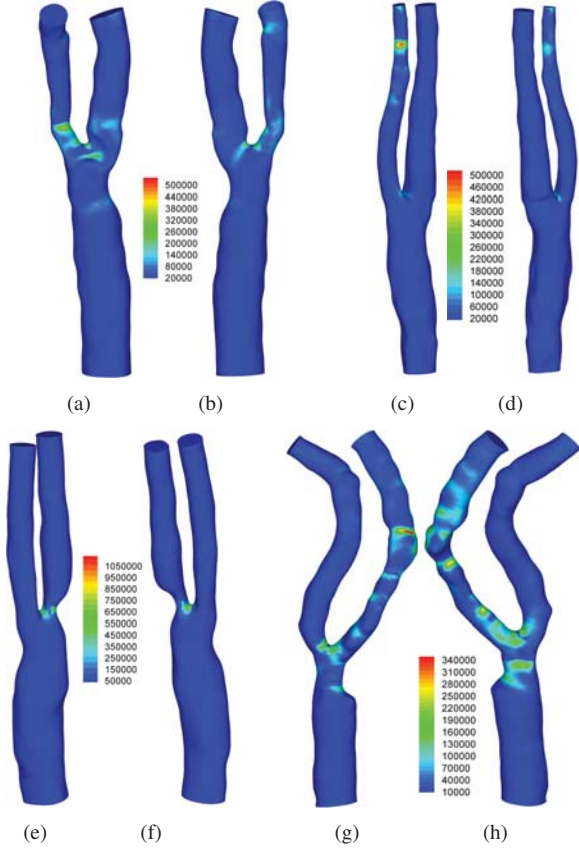
The distribution of WSSG is given in Figure 10. From the plot it is clear that in general the distributions of WSSG is in agreement with that of time-averaged WSS and maximum WSSTG. Although the peak of all three parameters occur in close proximity, the regions of high WSSG, WSSTG and WSSTA are not entirely coincident. In the two carotids with a stenosis, the predicted WSSG values are significantly higher, compared to P02R and P03L which do not.

WSSG is the third wall parameter that is negatively correlated to increased intima media thickness [47]. However, this correlation was only found in the CCA and not in the ICA. The ECA correlation was not examined. The work of Barbee *et al* [21] examined (using atomic force microscopy) the surfaces of living endothelial cells in a culture. They found that both shear stress and the spatial gradient of the wall shear stress induced alignment between the endothelial cells. With alignment, the smooth surface of unsheared cells was transformed into a surface exhibiting ridges extending in the direction of the flow within 24 hours. Therefore, while no correlation was found for the subjects studied, the WSSG distribution within the ICA

and ECA may still be relevant. While the work of Glor *et al* [10] found that while the WSSG distribution for a particular patient is highly reproducible on scans taken several weeks apart, the magnitudes were not. This also applied to time-averaged WSS and WSSTG. They concluded this is due to two factors. Accurate segmentation and meshing is required to capture these magnitudes, but also the waveform itself may alter significantly depending on condition of the patient.

The oscillatory shear index (OSI) originally introduced in [24] and adapted for general three dimensional use in [14] is used to quantify the transient shear stress dynamics experienced by the endothelial cells. The OSI is a ratio of the absolute wall shear stress and the mean wall shear stress. The mean wall shear stress is calculated as the magnitude of the time-averaged surface traction vector $\tau_{mean}$ which is defined as

$$\tau_{mean} = \left\| \frac{1}{T} \int_0^T \mathbf{t_s} dt \right\| \tag{24}$$

and the oscillatory shear index is defined by [14]

$$OSI = \frac{1}{2}\left(1 - \frac{\tau_{mean}}{\tau_{abs}}\right) \tag{25}$$

The oscillatory shear index will always lie within the range $0 \leq OSI \leq 0.5$ and does not take into account the magnitude of the shear stress vectors, it only accounts for WSS directions. The OSI quantifies the amount of time a point experiences flow away from the predominant axial direction such as cross or reverse flow within a cycle.

Although the clinical threshold for the OSI leading to a substantially increased risk of atherosclerotic lesions has not yet been fully determined, a correlation between the oscillating shear stress and the predisposition of lesion development has been reported [38, 44].

Figure 11 gives the distribution of the oscillating shear index for all cases. In the CCA of P01R, the OSI values are minimal, with only a small region displaying mildly elevated values. This region corresponds to the only region within P01R displaying WSSTA values of less than 5 dyne/cm$^2$. These values together with low WSSG and WSSTG (less than 1000 dyne/cm$^3$ and 1000 dyne/cm$^2$s respectively) indicate a potential region of atherogenesis. While the oscillating shear index at this point is low, atherosclerosis is believed to develop in regions of low or oscillatory shear stresses. As outlined in [8], the "destabilising" components within the plaque composition would be greater in low rather than oscillatory shear. In the ECA, a region of high OSI extends from the inner wall of the sharp curvature downstream to the outlet. This wall region corresponds to low velocities within the flow due to the curvature skewing the flow to the outer wall, resulting in low (10-15 dyne/cm$^2$) time-averaged WSS. High OSI is also predicted within the ICA along the anterior wall.

**Figure 11 OSI distribution. (a,b) P01R, (c,d) P02R, (e,f) P02L, (g,h) P03L.**



(a)       (b)       (c)       (d)



(e)       (f)       (g)       (h)
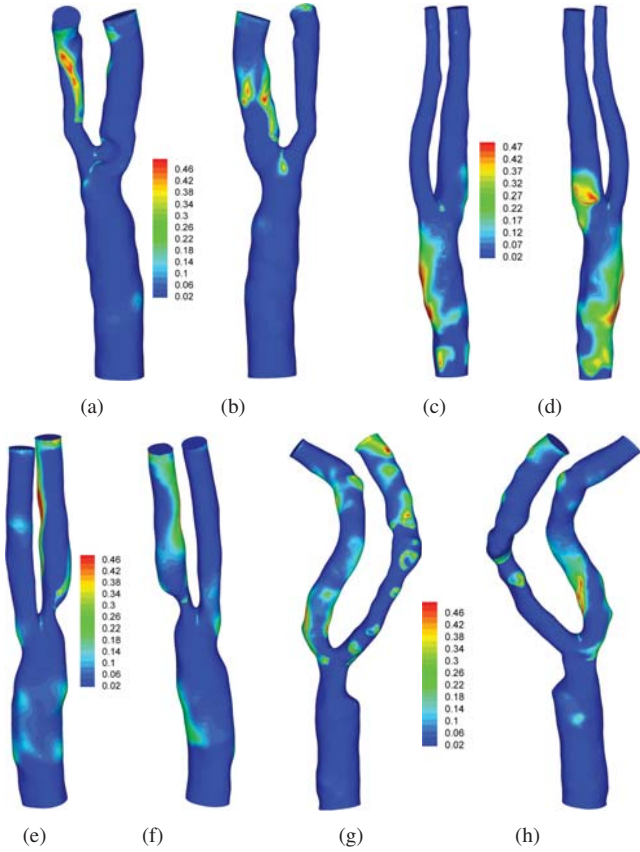
In P02R, the oscillating shear index is high in the majority of the CCA, while absent from the ECA due to the narrow width of the artery and it's relatively shallow curvature avoiding the induction of skewed or swirling flow. As in the CCA, the region in the ICA experiencing high OSI is distal to a local narrowing and along the outer wall. This is in good agreement with that of [20]. High OSI is also predicted within the ICA and ECA of both P02L and P03L.

The oscillatory shear index does not necessarily always provide a good indication of atherogenesis [47]. In order to back up the OSI prediction, another directional quantity called wall shear stress angle deviation (WSSAD) can be employed. This is used to summarise the spatial variation of the mean shear stress direction. It can be used to evaluate the varying flow directions if adjacent surface nodes are approximately equidistant. It is defined as

$$\text{WSSAD} = \frac{1}{T} \int_0^T \left( \frac{1}{A_i} \int_S \phi_i dA_i \right) dt \qquad (26)$$

where $A_i$ represents the control volume surface area, which is defined as the sum of the connected element areas for node $i$ and $\phi_i$ is defined as

$$\phi_i = \arccos \left( \frac{\boldsymbol{\tau}_i \cdot \boldsymbol{\tau}_j}{\|\boldsymbol{\tau}_i\| \cdot \|\boldsymbol{\tau}_j\|} \right) \qquad (27)$$

where $\boldsymbol{\tau}_i$ represents the surface stress vector at the point of interest and $\boldsymbol{\tau}_j$ denotes the surrounding surface stress vectors. $j = 1 : n$ where $n$ is the number of connected points to $i$.

A closely related parameter is the time-averaged wall shear stress angle gradient (WSSAG). It is employed as a mesh independent wall shear stress directional parameter [23]. It is defined as

$$\text{WSSAG} = \frac{1}{T} \int_0^T \left| \frac{1}{A_i} \int_S \nabla \phi_i dA_i \right| dt \qquad (28)$$

As a time-averaged parameter it can identify locally high values of WSSAG which are sustained over the cardiac cycle. High WSSAG can be an indicator of atherogenesis [19].

**Figure 12 WSSAD distribution. (a,b) P01R, (c,d) P02R, (e,f) P02L, (g,h) P03L.**



(a)       (b)       (c)       (d)



(e)       (f)       (g)       (h)
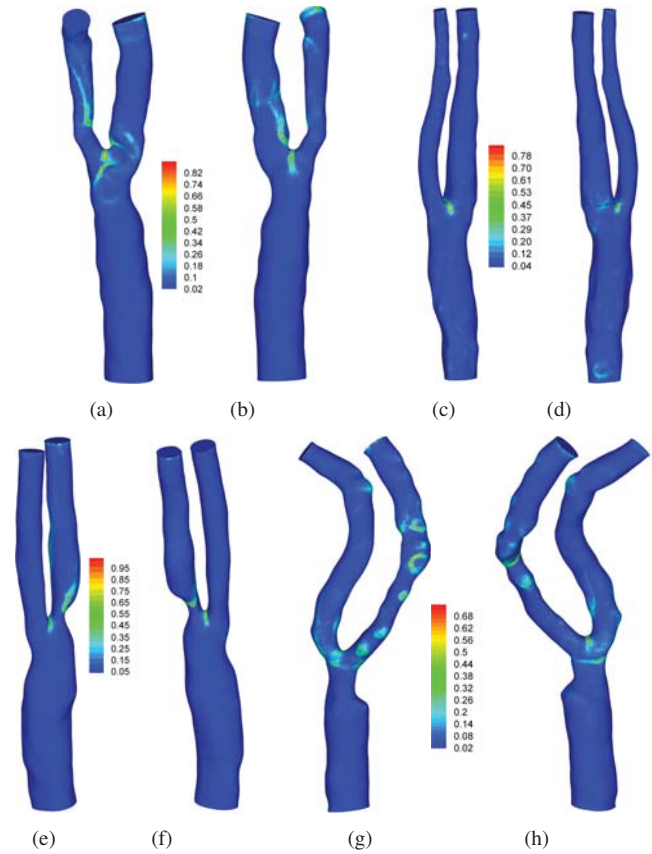
The distributions of wall shear stress angle deviation (WSSAD) and wall shear stress angle gradient (WSSAG) are virtually identical and hence shall be discussed together. The distribution of WSSAD is presented in Figure 12 and WSSAG in Figure 13. From the figures it is clear that in contrast to the OSI parameter, only small elongated regions experience high or elevated WSSAD (and hence WSSAG). In P03L, starting in the CCA and extending into the ECA, small regions of elevated WSSAD are predicted.

**Figure 13 WSSAG distribution. (a,b) P01R, (c,d) P02R, (e,f) P02L, (g,h) P03L.**



(a)　　　　(b)　　　　(c)　　　　(d)

(e)　　(f)　　　　(g)　　　　(h)
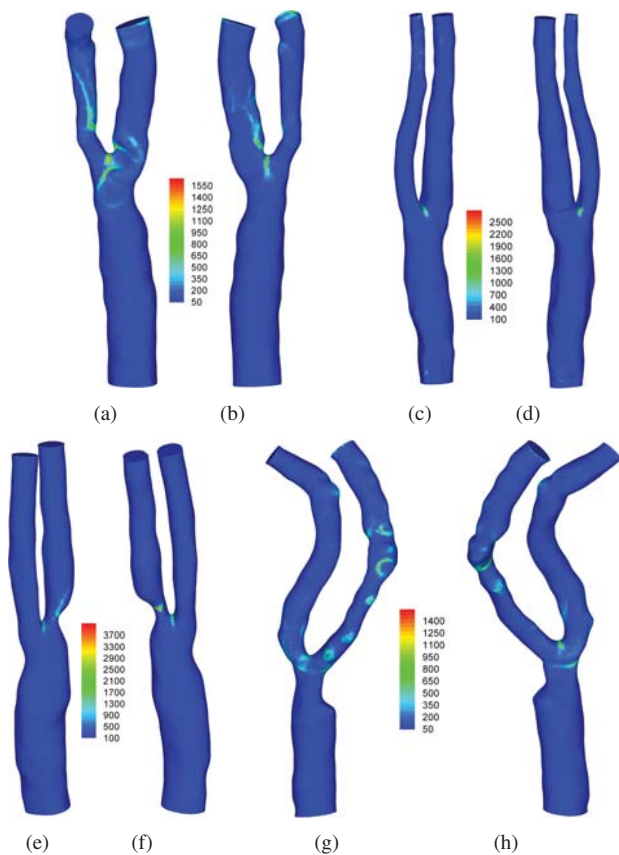
These correspond well to the outline of a region of high OSI. In the remainder of the CCA, WSSAD remains minimal. In P02R, only mildly elevated WSSAD values are predicted away from the flow divider. These elevated values are predicted along the anterior wall of the ICA prior to a local widening of the artery. Peak WSSAD values are predicted at the flow divider, which is in excellent agreement with that of P03L. The distribution of WSSAD in P01R contains significant regions of elevated or high predicted values. Three small regions are located near the flow divider. Elevated regions also extend along the inner wall of the ECA downstream of the sharp curvature. In the CCA, the WSSAD values are minimal which is in good agreement with P02R and P03L. In P02L, the flow divider experiences high WSSAD and WSSAG as in the previous three carotids. However, the location of peak WSSAG values does not coincide either with the peak WSSAD or the flow divider.

In order to understand the differences between the WSSAD/WSSAG distributions and OSI, it is worth considering what the respective parameter represents. While OSI is concerned with deviation of the flow direction from the historial mean shear stress direction at a node, the (time-averaged) WSSAD parameter is concerned with the shear stress directions of the surrounding region at any time instance. Thus, the OSI parameter provides information on

transient oscillation whereas the WSSAD parameter provides data on spatial oscillation in the region. Where the two parameters coincide in predicting elevated or high values then the oscillations are predicted to be both transient and spatial. High values of WSSAD and WSSAG may be considered normal at the flow divider as the flow is being directed into two different arteries. Glor *et al* [10] demonstrated that both qualitatively and quantitatively the parameters of OSI and WSSAD were highly reproducible (>90%) on scans taken weeks apart, ensuring that the predicted results for these parameters are relevant and reproducible.

With the study of only four carotid geometries it is possible to see factors that influence the distributions of the derived parameters. It is clear that a region distal to the flow divider is a potential region of atherosclerotic plaque formation (in 2 out of 4 of these carotids and 3 out of 4 in [20]). With the remaining two carotids already subjected to a stenosis proximal to this region the implications are even clearer. The predicted WSS values are higher than those from existing literature due to the use of a high resolution boundary layer. The CCA in all subjects experienced relatively low time-averaged WSS although only a small region in P01R experienced less than 5 dyne/cm$^2$ compared to more significant regions in P02R, P02L and P03L. Flow within the ICA and ECA in general is disturbed and swirling, although this is reduced with smaller bifurcation angle differences between the relative arterial axes. Downstream of the bifurcation, the time-averaged WSS, WSSG and WSSTG values tend to be higher (and locally significantly so) than in the CCA. At the bifurcation itself, the WSSAD and WSSAG values are expected to be high since flow is dividing between the ICA and ECA. A high WSSTA, along with WSSG and WSSTG is expected at the apex although in all four carotids the location is not central and tends to either the ICA or ECA. While the apex value of time-averaged WSS is high, the peak location is dependent upon any stenosis present within the domain. If the stenosis is proximal to the bifurcation as it is in P01R and P02L, then the peak time-averaged values are significantly increased to potentially life threatening levels due to increased risk of rupture.

## Conclusions

The numerical simulation of blood flow through four subject-specific carotids (two with moderate stenosis) has been presented. These simulations utilised high resolution meshes with near-wall refinement. Within P01R and P02L, the predicted high shear stress (peak WSSTA of 467 and 805 dyne/cm$^2$ respectively) is sufficient to activate platelets and micro-particle formation as well as enhancing platelet thrombus formation. This demonstrates the need for this near-wall refinement in order to accurately assess the wall shear stress derived haemodynamic wall parameters. The investigations also determined that a region distal to the flow divider is a potential region of atherosclerotic plaque formation for P02R and P03L. This region corresponded to a stenosis in P01R and P02L. The

use of subject-specific transient flow profiles would further enhance the model.

## Acknowledgements

## References

[1] *Coronary Heart Disease Statistics*. British Heart Foundation, 2010.

[2] A. Augst, B.Ariff, S. M. Thom, X.Y.Xu, and A.D.Hughes. Analysis of complex flow and the relationship between blood pressure, wall shear stress and intima-media thickness in the human carotid artery. *Am J Physiol Heart Circ Physiol*, 293:1031–1037, 2007.

[3] B. Berk. Atheroprotective signaling mechanisms activated by steady laminar flow in endothelial cells. *Circulation*, 117:1082–1089, 2008.

[4] B. C. Berk, J.-I. Abe, W. Min, J. Surapisitchat, and C. Yan. Endothelial atheroprotective and anti-inflammatory mechanisms. *Annals of New York Acadamy of Sciences*, 947:93–111, 2001.

[5] R. Bevan, P. Nithiarasu, R. V. Loon, I. Sazonov, H. Luckraz, and A. Garnham. Application of a locally conservative Galerkin (LCG) method for modelling blood flow through a patient-specific carotid bifurcation. *International Journal for Numerical Methods in Fluids*, DOI: 10.1002/fld.2313.

[6] M. L. Bots, A. Hofman, P. T. V. M. D. Jong, and D. E. Grobbee. Common carotid intima-media thickness as an indicator of atherosclerosis at other sites of the carotid artery the Rotterdam Study. *Annals of Epidemiology*, 6(2):147–153, 1996.

[7] J. R. Buchanan, C. Kleinstreuer, S. Hyun, and G. A. Truskey. Hemodynamics simulation and identification of susceptible sites of atherosclerotic lesion formation in a model abdominal aorta. *Journal of Biomechanics*, 36:1185–1196, 2003.

[8] C. Cheng, D. Tempel, R. van Haperen, A. van der Baan, F. Grosveld, M. Daemen, R. Krams, and R. de Crom. Atherosclerotic lesion size and vulnerability are determined by patterns of fluid shear stress. *Circulation*, 113:2744–2753, 2006.

[9] S. Ebrahim, O. Papacosta, P. Whincup, G. Wannamethee, M. Walker, A. Nicolaides, S. Dhanjil, M. Griffin, G. Belcaro, A. Rumley, and G. Lowe. Carotid plaque, intima media thickness, cardiovascular risk factors, and prevalent cardiovascular disease in men and women : The british regional heart study. *Stroke*, 30:841–850, 1999.

[10] F. P. Glor, Q. Long, A. D. Hughes, A. D. Augst, B. Ariff, S. A. M. Thom, P. R. Verdonck, and X. Y. Xu. Reproducibility study of magnetic resonance image-based computational fluid dynamics prediction of carotid bifurcation flow. *Annals of Biomedical Engineering*, 31:142–151, 2003.

[11] H. Groen, F. Gijsen, A. van der Lugt, M. Ferguson, T. Hatsukami, A. van der Steen, C. Yuan, and J. Wentzel. Plaque rupture in the carotid artery is localized at the high shear stress region: A case report. *Stroke*, 38:2379–2381, 2007.

[12] H. Groen, L. Simons, Q. van den Bouwhuijsen, E. Bosboom, F. Gijsen, A. van der Giessen, F. van de Vosse, A. Hofman, A. van der Steen, J. Witteman, A. van der Lugt, and J. Wentzel. MRI-based quantification of outflow boundary conditions for computational fluid dynamics of stenosed human carotid arteries. *Journal of Biomechanics*, 43:2332–2338, 2010.

[13] O. Hassan, K. Morgan, K. Probert, and J. Peraire. Unstructured tetrahedral mesh generation for three-dimensional viscous flows. *International Journal for Numerical Methods in Engineering*, 39:549–567, 1996.

[14] X. He and D. Ku. Pulsatile flow in the human left coronary artery bifurcation: Average conditions. *Journal of Biomechanical Engineering*, 118:74–82, 1996.

[15] D. Holdsworth, C. Norley, R. Frayne, D.A.Steinman, and B.K.Rutt. Characterization of common carotid artery blood-flow waveforms in normal human subjects. *Physiological Measurement*, 20:219–240, 1999.

[16] P. Holme, U. Orvim, M. Hamers, N. Solum, F.R.Brosstad, R. Barstad, and K. Sakariassen. Shear-induced platelet activation and platelet microparticle formation at blood flow conditions as in arteries with a severe stenosis. *Arteriosclerosis Thrombosis and Vascular Biology*, 17:646–653, 1997.

[17] J. Hwang, M. H. Ing, A. Salazar, B. Lassègue, K. Griendling, M. Navab, A. Sevanian, and T. K. Hsiai. Pulsatile versus oscillatory shear stress regulates nadph oxidase subunit expression. *Circulation Research*, 93:1225–1232, 2003.

[18] J. Hwang, A. Saha, Y. C. Boo, G. P. Sorescu, J. S. McNally, S. M. Holland, S. Dikalov, D. P. Giddens, K. K. Griendling, D. G. Harrison, and H. Jo. Oscillatory shear stress stimulates endothelial production of from p47phox-dependent nad(p)h oxidases, leading to monocyte adhesion. *Journal of Biological Chemistry*, 278:47291–47298, 2003.

[19] S. Hyun, C. Kleinstreuer, P. Longest, and C.Chen. Particle-hemodynamics simulations and design options for surgical reconstruction of diseased carotid artery bifurcations. *Journal of Biomechanical Engineering*, 126:188–195, 2004.

[20] M. R. Kaazempur-Mofrad, A. G. Isasi, H. F. Younis, R. C. Chan, D. P. Hinton, G. Sukhova, G. M. LaMuraglia, R. T. Lee, and R. D. Kamm. Characterization of the atherosclerotic carotid bifurcation using MRI finite element modeling, and histology. *Annals of Biomedical Engineering*, 32:932–946, 2004.

[21] K.A.Barbee, P.F.Davies, and R.Lal. Shear stress-induced reorganization of the surface topography of

living endothelial cells imaged by atomic force microscopy. *Circulation Research*, 74:163–171, 1994.

[22] G. Karner, K. Perktold, M. Hofer, and D. Liepsch. Flow characteristics in an anatomically realistic compliant carotid artery bifurcation model. *Computer Methods in Biomechanics and Biomedical Engineering*, 2(3):171–185, 1998.

[23] C. Kleinstreuer. *Biofluid Dynamics Principles and Selected Applications*. Taylor & Francis, 2006.

[24] D. N. Ku, D. P. Giddens, C. K. Zarins, and S. Glagov. Pulsatile flow and atherosclerosis in the human carotid bifurcation - positive correlation between plaque location and low and oscillating shear-stress. *Atherosclerosis*, 5(3):293–302, 1985.

[25] S. E. Lee, S.-W. Lee, P. F. Fischer, H. S. Bassiouny, and F. Loth. Direct numerical simulation of transitional flow in a stenosed carotid bifurcation. *Journal of Biomechanics*, 41:2551–2561, 2008.

[26] S.-W. Lee, L. Antiga, J. D. Spence, and D. A. Steinman. Geometry of the carotid bifurcation predicts its exposure to disturbed flow. *Stroke*, 39:2341–2347, 2008.

[27] M. Lei, C. Kleinstreuer, and J. A. Jr. Geometric design improvements for femoral graft-artery junctions mitigating restenosis. *Journal of Biomechanics*, 29:1605–1614, 1996.

[28] A. Mailhac, J.J.Badimon, J.T.Fallon, A. Fernandez-Ortiz, B. Meyer, J. Chesebro, V. Fuster, and L.Badimon. Effect of an eccentric severe stenosis on fibrin(ogen) deposition on severely damaged vessel wall in arterial thrombosis. relative contribution of fibrin(ogen) and platelets. *Circulation*, 90:988–996, 1994.

[29] I. Marshall, P. Papathanasopoulou, and K. Wartolowska. Carotid flow rates and flow division at the bifurcation in healthy volunteers. *Physiological Measurement*, 25:691–697, 2004.

[30] J. Milner, J. Moore, B. Rutt, and D. Steinman. Hemodynamics of human carotid artery bifurcations: Computational studies with models reconstructed from magnetic resonance imaging of normal subjects. *Journal of vascular surgery*, 28:143–156, 1998.

[31] T. Nagel, N. Resnick, C. F. D. Jr, and M. A. G. Jr. Vascular endothelial cells respond to spatial gradients in fluid shear stress by enhanced activation of transcription factors. *Arterisoscelerosis, Thrombosis, and Vascular Biology*, 19:1825–1834, 1999.

[32] K. T. Nguyen, C. D. Clark, T. J. Chancellor, and D. V. Papavassiliou. Carotid geometry effects on blood flow and on risk for vascular disease. *Journal of Biomechanics*, 41:11–19, 2008.

[33] P. Nithiarasu. An efficient artificial compressibility (AC) scheme based on the charcteristic based split (CBS) method for incompressible flows. *International Journal for Numerical Methods in Engineering*, 56:1815–1845, 2003.

[34] P. Nithiarasu. A matrix free fractional step method

for static and dynamic incompressible solid mechanics. *Int. J. Comp. Meth. Eng. Sci and Mech.*, 7:369–380, 2006.

[35] P. Nithiarasu, R. Codina, and O. C. Zienkiewicz. The characteristic based split scheme - a unified approach to fluid dynamics. *International Journal for Numerical Methods in Engineering*, 66:1514–1546, 2006.

[36] P. Nithiarasu, J. S. Mathur, N. P. Weatherill, and K. Morgan. Three dimensional incompressible flow calculations using the characteristic based split (CBS) scheme. *International Journal for Numerical Methods in Fluids*, 44:1207–1229, 2004.

[37] P. Nithiarasu and O. C. Zienkiewicz. Analysis of an explicit and matrix free fractional step method for incompressible flows. *Computer Methods in Applied Mechanics and Engineering*, 195:5537 – 5551, 2006.

[38] S. Oyre, E. M. Pedersen, S. Ringgaard, P. Boesiger, and W. P. Paaske. In vivo wall shear stress measured by magnetic resonance velocity mapping in the normal human abdominal aorta. *European Journal of Vascular and Endovascular Surgery*, 13:263–271, 1997.

[39] P. Papathanasopoulou, S. Zhao, U. Köhler, M. B. Robertson, Q. Long, and P. Hoskins. MRI measurement of time-resolved wall shear stress vectors in a carotid bifurcation model, and comparison with CFD predictions. *Journal of Magnetic Resonance Imaging*, 17:153–162, 2003.

[40] K. Sakariassen, P. Holme, U. Orvim, R. Barstad, N.O.Solum, and F.R.Brosstad. Shear-induced platelet activation and platelet microparticle formation in native human blood. *Thrombosis Research*, 92:S33–S41, 1998.

[41] P. H. Saksono, P. Nithiarasu, and I. Sazonov. Computational flow studies in a subject-specific human upper airway using one-equation turbulence model. influence of the nasal cavity. *Int. J. Numer. Meth. Engng*, Submitted 2010.

[42] I. Sazonov, D. Wang, O. Hassan, K. Morgan, and N. Weatherill. A stitching method for the generation of unstructured meshes for use with co-volume solution techniques. *Computer Methods in Applied Mechanics and Engineering Corresponding*, 195:13–16, 1826–1845, 2006.

[43] I. Sazonov, S. Yeo, R. Bevan, X. Xie, R. van Loon, and P. Nithiarasu. Modelling pipeline for subject-specific arterial blood flow - a review. *International Journal for Numerical Methods in Biomedical Engineering*, DOI: 10.1002/cnm.1446.

[44] Y. Tardy, N. Resnick, T. Nagel, M. A. G. Jr, and C. F. D. Jr. Shear stress gradients remodel endothelial monolayers in vitro via a cell proliferation-migration-loss cycle. *Arteriosclerosis, Thrombosis, and Vascular Biology*, 17:3102–3106, 1997.

[45] T.E.Tezduyar, S. Sathe, T. Cragin, B. Nanna, B. Conklin, J. Pausewang, and M. Schwaab. Modelling of fluid-structure interactions with the space-time fi-

nite elements: Arterial fluid mechanics. *International Journal for the Numerical Methods in Fluids*, 54:901–922, 2007.

[46] O. Traub and B. Berk. Laminar shear stress : Mechanisms by which endothelial cells transduce an atheroprotective force. *Arteriosclerosis Thrombosis and Vascular Biology*, 18:677–685, 1998.

[47] S. J. Vermeersch, F. P. Glor, L. A. Crowe, B. Ariff, M. Bol, P. Segers, A. D. Hughes, X. Y. Xu, T. SMcG, D. N. Firmin, and P. R. Verdonck. Relationship between carotid artery intima-media thickness and wall shear stress derived parameters. *Computer Methods in Biomechanics and Biomedical Engineering*, 8(4):279–280, 2005.

[48] N. Weatherill and O.Hassan. Effcient three–dimensional delaunay triangulation with automatic point creation and imposed boundary constraints. *International Journal for Numerical Methods in Engineering*, 37:2005–2040, 1994.

[49] H. F. Younis, M. R. Kaazempur-Mofrad, R. C. Chan, A. G. Isasi, D. P. Hinton, A. H. Chau, L. A. Kim, and R. D. Kamm. Hemodynamics and wall mechanics in human carotid bifurcation and its consequences for atherogenesis - investigation of inter-individual variation. *Biomechanics and Modeling in Mechanobiology*, 3:17–32, 2004.

[50] O. C. Zienkiewicz and R. Codina. A general algorithm for compressible flow and incompressible flow - part I. the split characteristic-based scheme. *International Journal for Numerical Methods in Fluids*, 20:869–885, 1995.

[51] O. C. Zienkiewicz, K. Morgan, B. V. K. S. Sai, R. Codina, and M. Vazquez. A general algorithm for compressible flow - part II. tests on the explicit form. *International Journal for Numerical Methods in Fluids*, 20:887–913, 1995.

[52] O. C. Zienkiewicz, R. L. Taylor, and P. Nithiarasu. *The finite element method for fluid Dynamics*. Elsevier Butterworth Heinemann, London, 2005.